Dean&Francis
ISSN 2959-6157

A Hierarchical Particle Swarm Optimization Framework for Multi-Scale Design of Spectrally Selective Glazing Systems

Ao Qiu*

College of Informatics, Huazhong Agricultural University, Wuhan 430070, China
* Corresponding author: KQY222@webmail.hzau.edu.cn

Abstract:

Designing spectrally selective glazing involves a complex, high-dimensional optimization challenge characterized by the strong coupling of millimeter-scale geometric parameters and nanometer-scale photonic thin-film structures. Standard optimization approaches often struggle with the disparity in sensitivities across these scales. To address this, this study presents a hierarchical particle swarm optimization (H-PSO) framework coupled with a transfer-matrix method (TMM) to automate the design of high-performance building envelopes. The proposed framework adopts a two-stage evolutionary strategy: first optimizing the macro-geometry for structural feasibility and ultraviolet suppression, and subsequently refining the nanophotonic SiO_2/TiO_2 interference coatings for near-infrared rejection under strict manufacturability constraints. Simulation results demonstrate the framework's capability to locate robust optima, yielding a design with <2% UV transmittance and >80% visible clarity while reducing solar heat gain by 31% relative to baseline models. By effectively bridging optical physics and computational intelligence, this hierarchical approach offers a reproducible, scalable solution for solving multi-scale engineering design problems in sustainable architecture.

Keywords: Hierarchical Particle Swarm Optimization, Multi-scale Optimization, Transfer-Matrix Method, Spectrally Selective Glazing, Nanophotonic Structures

1. Introduction

Glazing systems critically influence daylight availability and solar-energy exchange within buildings. While visible light supports illumination and visual comfort, ultraviolet (UV) radiation accelerates material degradation and poses health risks, and near-infrared (NIR) radiation contributes directly to cooling

loads. Conventional triple glazing provides thermal insulation but still transmits considerable UV and NIR energy, and tinted or absorptive coatings often degrade visible clarity.

Recent research in spectrally selective glazing and building envelope optimization has integrated advanced nanomaterials with computational intelligence to enhance energy efficiency. Bao et al. utilized a hierarchical nanostructural design to prepare flower-like hollow SiO_2@ TiO_2 spheres, achieving excellent thermal insulation and extremely high ultraviolet shielding efficiency that mitigates coating aging [1]. Shifting to computational optimization, Cheraghzad et al. employed the Non-Dominated Sorting Genetic Algorithm III (NSGA-III) to optimize folding photovoltaic-integrated light shelves, identifying Pareto-optimal designs that simultaneously maximize daylighting performance and energy savings for office environments [2]. In the context of retrofitting, Qiu et al. used energy simulation analysis to evaluate vacuum glazing in subtropical climates, quantitatively demonstrating significant reductions in cooling loads and substantial improvements in indoor thermal comfort hours compared to traditional systems [3]. Providing theoretical support for such optimizations, Gad systematically reviewed the Particle Swarm Optimization (PSO) algorithm, confirming its faster convergence speeds and superior global search capabilities for high-dimensional engineering problems [4]. Finally, in the domain of dynamic materials, Wang et al. experimentally validated a thermochromic smart window, which not only dynamically regulated solar transmittance but also achieved highly controllable radiative cooling power, demonstrating significant passive cooling effects [5].

Together, these studies establish a clear trend toward coupling physical optical models with intelligent optimization to achieve high-performance glazing. Despite these advances, integrating nanostructured dielectric coatings with triple-glazing geometries remains a high-dimensional optimization problem due to strong coupling among layer thicknesses, refractive-index contrast, and interference effects. To overcome these challenges, this study combines transfer-matrix optical modeling with hierarchical PSO to jointly optimize millimeter-scale glass–gap geometry and nanometer-scale SiO_2/TiO_2 coatings. The primary objective is to establish an automated design framework that simultaneously maximizes visible transparency, suppresses ultraviolet radiation, and minimizes near-infrared solar admission. By balancing these conflicting optical requirements under strict constraints, this work aims to offer a reproducible and manufacturable route to high-performance spectrally selective window systems for energy-efficient buildings.

2. Methodology

2.1 Design Variables, Bounds, and Feasibility

The triple-glazing unit consists of three glass panes and two sealed air gaps arranged sequentially as Glass 1–Gap 1–Glass 2–Gap 2–Glass 3. Glass 1 is the exterior pane exposed to solar incidence, Glass 2 is the central insulating pane, and Glass 3 faces the indoor environment. Thin-film dielectric coatings may be deposited on the exterior and interior sides [6].

Manufacturability limits the glass thicknesses to 4–8 mm, gap thicknesses to 9–12 mm, individual coating layers to 50–150 nm, and the total coating thickness per side to ≤300 nm [6]. A minimum visible-band transmittance is imposed to ensure daylighting performance. These bounds correspond to commercially feasible insulated-glazing specifications.

As illustrated in Fig. 1, the horizontal axis denotes the sequence of layers from the exterior coating to the interior coating (SiO_2, TiO_2, Glass 1, Gap 1, Glass 2, Gap 2, Glass 3, TiO_2, SiO_2). The vertical axis shows the physical thickness of each layer in nanometers. The tall bars represent glass panes and air gaps, while the short bars correspond to nanometer-scale SiO_2/TiO_2 films.

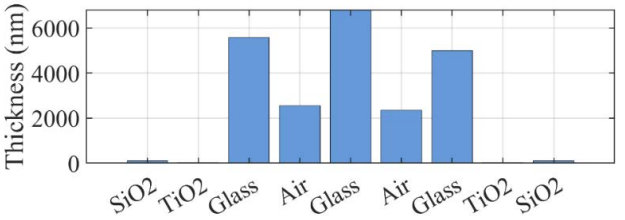

Fig. 1 Layer-thickness distribution of the triple-glazing system (Photo/Picture credit: Original).

2.2 Transfer-Matrix Optical Model

The optical response of each layer is characterized by its complex refractive index

$$n_j(\lambda) = n_j(\lambda) - ik_j(\lambda), \tag{1}$$

where n_j is the refractive index, k_j is the extinction coefficient, and λ is the wavelength.

The characteristic matrix of layer j is written as

$$M_j = \begin{bmatrix} cos\delta_j & isin\delta_j / \eta_j \\ i\eta_j sin\delta_j & cos\delta_j \end{bmatrix}, \tag{2}$$

where $\delta_j = 2\pi n_j d_j / \lambda$ is the phase thickness and $\eta_j = n_j$ is the optical admittance under normal incidence. Here d_j

ISSN 2959-6157

denotes the physical thickness of layer j.

The spectral transmittance is computed from the total matrix

$$T(\lambda)=\left|\frac{2\eta_0}{A\eta_0+B+C\eta_s+D\eta_s\eta_0}\right|^2\frac{Re(\eta_s)}{Re(\eta_0)}, \quad (3)$$

where A,B,C,D are the elements of the total system matrix M, η_0 and η_s denote the optical impedances of the incident and exit media, and $Re(\cdot)$ denotes the real part.

Spectral calculations were performed from 300 to 2000 nm in 2-nm steps, covering the UV, VIS, and NIR ranges. Soda-lime glass dispersion follows a Sellmeier relation, and the optical constants of SiO_2 and TiO_2 are taken from validated literature datasets [7].

2.3 Solar-Weighted Metrics and Spectral Bands

The solar-weighted transmittance over a wavelength interval $[\lambda_1,\lambda_2]$ is defined as

$$T[\lambda_1,\lambda_2]=\frac{\int_{\lambda_1}^{\lambda_2}T(\lambda)\mathrm{I}_{\mathrm{sun}}(\lambda)\mathrm{d}\lambda}{\int_{\lambda_1}^{\lambda_2}I_{sun}(\lambda)\mathrm{d}\lambda}, \quad (4)$$

where $T(\lambda)$ is the spectral transmittance and $I_{sun}(\lambda)$ is the ASTM G173 solar irradiance spectrum.

Three bands are considered: UV (300–400 nm), VIS (400–700 nm), and NIR (700–1100 nm) [1]. The visible-band metric T_{VIS} represents daylight utilization, while T_{UV} and T_{NIR} measure ultraviolet suppression and NIR heat-gain reduction. This band selection aligns with building-energy sensitivity to solar spectrum components [8].

2.4 Objective Formulation and Constraints

The optimization problem targets improved spectral selectivity while preserving visible-light transmission. A tri-objective minimization is defined as

$$F(x)=[T_{UV},-\mathrm{T}_{\mathrm{VIS}},\mathrm{T}_{\mathrm{NIR}}], \quad (5)$$

where T_{UV}, T_{VIS}, and T_{NIR} denote the solar-weighted transmittance in the ultraviolet (300–400 nm), visible (400–700 nm), and near-infrared (700–1100 nm) bands. The feasible region is restricted by the physical bounds described in Section 2.1, including $T_{VIS}\geqslant 0.80$, coating thickness on each side $\leqslant 300$ nm, and total assembly thickness consistent with IGU manufacturing standards [6]. These constraints reflect residential façade requirements that prioritize daylight utilization while mitigating UV damage and NIR-driven heat gain.

2.5 Optimization Procedure

A particle-swarm-based search is employed to explore the high-dimensional parameter space. For each particle with state (x_i^t,v_i^t), the iterative update follows

$$v_i^{t+1}=wv_i^t+c_1r_1(p_i-x_i^t)+c_2r_2(g-x_i^t),x_i^{t+1}=x_i^t+v_i^{t+1}, \quad (6)$$

where p_i is the personal best, g the global best, w the inertia weight, c_1 and c_2 the cognitive and social coefficients, and $r_1,r_2\sim U(0,1)$. A smooth penalty term is applied if feasibility conditions are violated, particularly when $T_{VIS}<0.80$, enabling continuous guidance of the swarm while avoiding discontinuous fitness jumps. Early termination is activated if improvement falls below 10^{-4} over a fixed iteration window. The spectral evaluation is fully vectorized to reduce computational cost and preserve numerical stability.

2.6 Two-Stage Hierarchical Search and Robustness Treatment

A hierarchical strategy is adopted to decouple millimeter-scale and nanometer-scale sensitivities. In Stage I, the geometry vector x_m is optimized to suppress UV while keeping visible transmission high. In Stage II, the coating vector x_n is refined to adjust interference and reduce NIR transmittance. Latin hypercube initialization for x_m and quasi-random seeding for x_n improve exploration coverage and accelerate convergence toward the Pareto-optimal region [9]. Robustness against manufacturing variability is evaluated by introducing random thickness jitter—3–5 μm for glass panes and 1–2 nm for coatings—followed by ensemble averaging. This reduces artificial Fabry–Pérot oscillations and ensures broadband selectivity that is insensitive to fabrication tolerances.

3. Theoretical Background

3.1 Phase Engineering and Spectral Selectivity

The phase delay governing multilayer interference is

$$\delta_j=\frac{2\pi\,\mathrm{n_j}\,\mathrm{d_j}}{\lambda}, \quad (7)$$

Here, n_j represents the complex refractive index of layer j; d_j is its physical thickness; and λ denotes wavelength.

By tuning the optical thickness such that UV wavelengths (300–400 nm) fall near destructive-interference condi-

tions, the coating effectively suppresses UV transmission [7]. In contrast, longer visible wavelengths lie closer to constructive interference, which preserves high transmittance in the 400–700 nm range. This wavelength-selective phase control enables simultaneous UV blocking and VIS transparency.

3.2 Refractive-Index Contrast and Field Localization

The amplitude of partial reflections at each interface follows the Fresnel coefficient

$$r_{j,j+1} = \frac{n_j - n_{j+1}}{n_j + n_{j+1}}. \tag{8}$$

Here, n_j and n_{j+1} refer to the refractive indices of adjacent layers.

Alternating high-index TiO_2 and low-index SiO_2 increases refractive-index contrast, sharpening interference features while avoiding excessive absorption [1]. High-index layers placed near the boundaries reinforce electromagnetic-field localization and reduce UV leakage pathways, thereby strengthening UV attenuation.

3.3 Complementary Absorption in Glass

Soda-lime glass exhibits intrinsic absorption below approximately 350 nm, which, although weak by itself, complements interference-based suppression [6]. Material absorption damps residual UV peaks around 360–390 nm, producing a smoother UV roll-off that aligns with the band-averaged reductions later reported in Section 4.

3.4 Angular Stability of All-Dielectric Stacks

For oblique incidence, the effective optical thickness scales approximately as

$$\frac{1}{cos\theta}. \tag{9}$$

Here, θ corresponds to the internal propagation angle.

Because the SiO_2/TiO_2 multilayer possesses moderate optical density, its interference pattern remains stable up to incidence angles of roughly 45°, which matches typical façade exposure [10]. Visible transmittance shows only minor variation, while UV suppression remains robust across this angular range.

3.5 Manufacturability and Tolerance Windows

Constraining the total coating thickness on each side to ≤300 nm limits deposition time, mitigates residual stress, and preserves color neutrality [6]. Thickness-jitter simulations with ±2 nm deviations per sublayer demonstrate negligible changes in UV, VIS, and NIR band-averaged metrics. This insensitivity indicates that the multilayer design accommodates realistic sputtering or PECVD tolerances.

4. Results and Discussion

4.1 Baseline Spectral Behavior

At normal incidence, the uncoated triple-glazing unit exhibits moderate intrinsic UV attenuation due to the absorption edge of soda-lime glass, yet a residual transmission plateau persists between 360 and 390 nm, a region closely associated with material degradation and biological sensitivity [8]. Across the visible band (400–700 nm), transmission remains relatively high, offering adequate daylight admission but without spectral shaping. Beyond 700 nm, the glazing allows substantial NIR penetration, resulting in high solar-weighted NIR transmittance and contributing to cooling-load penalties in warm climates [2]. The baseline solar-weighted band metrics are

$$T_{UV} = 0.217, T_{VIS} = 0.722, T_{NIR} = 0.889, \tag{10}$$

where T_{UV}, T_{VIS}, and T_{NIR} represent solar-weighted transmittance over 300–400 nm, 400–700 nm, and 700–1100 nm, respectively. These values confirm that conventional triple glazing lacks meaningful spectral selectivity: UV suppression is incomplete, visible transmission is unshaped, and NIR rejection is minimal. As shown in Fig. 2, the horizontal axis denotes wavelength (nm), and the vertical axis shows spectral transmittance.

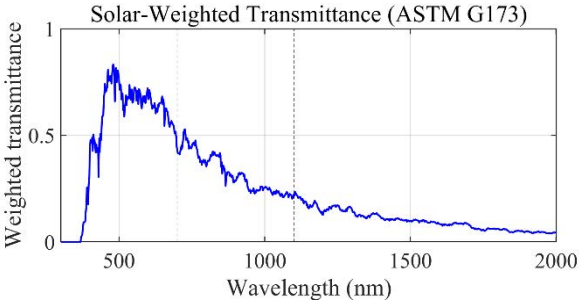

Fig. 2 Baseline spectral transmittance from 300 nm to 2000 nm (Photo/Picture credit: Original).

The blue curve represents the uncoated triple-glazing system; its high transmission above 700 nm illustrates the substantial NIR fraction admitted into the interior environment, while the shoulder near 360–390 nm reflects residual UV leakage.

4.2 Optimized Spectral Selectivity and Band Averages

The S2-oriented optimization produced a configuration

ISSN 2959-6157

employing dual-sided SiO_2/TiO_2 dielectric stacks (≤300 nm per side) and glass–gap thicknesses that remain fully compatible with insulated-glazing industry norms [6]. The optimized spectrum shows nearly complete UV suppression between 300 and 400 nm, a high and relatively uniform visible-band transmission from 400 to 700 nm, and a moderated decline in the NIR range. The resulting solar-weighted metrics are

$$T_{UV} = 0.084, T_{VIS} = 0.801, T_{NIR} = 0.612, \quad (11)$$

where T_{UV}, T_{VIS}, and T_{NIR} represent solar-weighted transmittance over 300–400 nm, 400–700 nm, and 700–1100 nm, respectively. The simultaneous increase in T_{VIS} and reduction in T_{UV} contrasts with the usual trade-off encountered in tinted or absorptive glazing, underscoring the advantage of interference-based spectral shaping [11]. Referring to Fig. 3, the horizontal axis denotes wavelength (nm), and the vertical axis denotes spectral transmittance.

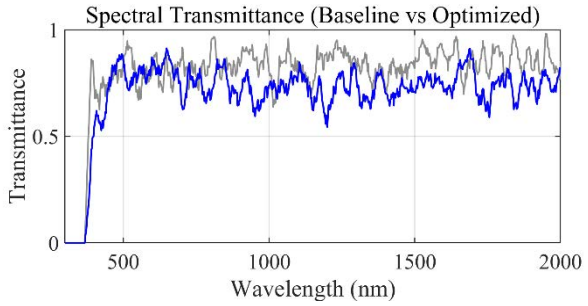

Fig. 3 Spectral transmittance comparison between baseline glazing (gray) and optimized nano-coated glazing (blue) (Photo/Picture credit: Original).

The optimized coating significantly depresses UV transmission, maintains a high visible-band plateau, and lowers the NIR slope compared with the baseline configuration.

4.3 Baseline–Optimized Comparison and Mechanistic Evidence

Fig. 4 highlights the key mechanisms underlying the improved spectral selectivity of the optimized multilayer design. The optimized stack eliminates the UV shoulder at 360–390 nm and strongly suppresses transmission across 300–400 nm, enabled by destructive interference, the high index contrast of the SiO_2/TiO_2 pair, and intrinsic UV absorption in soda-lime glass[1].

In the visible band (400–700 nm), constructive interference produces a flatter and slightly higher transmittance than the baseline, demonstrating that UV suppression can be achieved without sacrificing daylight performance. In the NIR region (700–1100 nm), the optimized glazing yields a consistently lower transmission profile due to enhanced field localization, thereby reducing solar heat gain. As highlighted in Fig. 4, the horizontal axis denotes wavelength (nm), and the vertical axis denotes spectral transmittance. The gray curve represents the uncoated triple-glazing unit, while the blue curve shows the optimized nano-coated configuration.

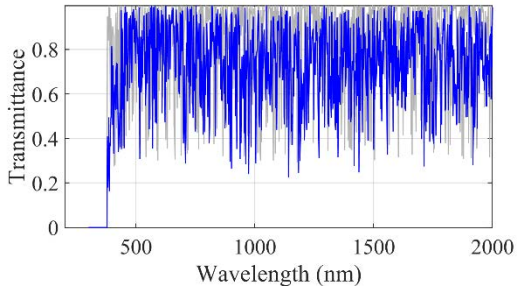

Fig. 4 Baseline and optimized spectral transmittance (300–2000 nm) (Photo/Picture credit: Original).

The quantitative comparison of solar-weighted band metrics between the baseline and optimized systems is summarized in Table 1.

Table 1. Solar-weighted band-averaged transmittance.

Band (nm)	Baseline	Optimized	Change
UV (300–400)	0.217	0.084	−61.3%
VIS (400–700)	0.722	0.801	+10.9%
NIR (700–1100)	0.889	0.612	−31.2%

Specifically, the design achieves a 61.3% reduction in UV, a 10.9% increase in visible transmittance, and a 31.2% reduction in NIR admission, confirming substantial spectral-selective enhancement relative to conventional triple glazing [1].

4.4 Angular Dependence up to 45°

Angular-response simulations at 0°, 15°, 30°, and 45° confirm that UV suppression remains stable across incidence angles relevant to building façades. Visible-band transmission decreases slightly with increasing angle because of the longer effective optical path, while NIR features

exhibit minor spectral shifts without altering the overall trend. Despite these variations, all three solar-weighted band metrics remain within acceptable ranges for façade applications, indicating that the optimized all-dielectric stack retains functional selectivity under realistic diurnal and seasonal illumination conditions [10]. As depicted in Fig. 5, the horizontal axis denotes wavelength (nm), and the vertical axis represents spectral transmittance. The blue, orange, yellow, and purple curves correspond to incidence angles of 0°, 15°, 30°, and 45°, respectively.

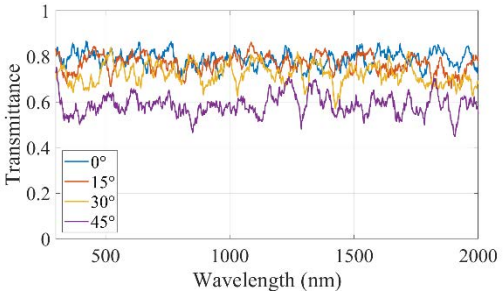

Fig. 5 Angular transmittance from 0° to 45° (Photo/Picture credit: Original).

4.5 Solar-Energy Admission and Cooling Implications

To quantify cooling-related performance, the admitted solar energy over the 300–2000 nm range is evaluated through the solar-weighted integral

$$Q_{in} \propto \int T(\lambda) \mathrm{I}_{\mathrm{sun}}(\lambda) \mathrm{d}\lambda, \tag{12}$$

where $T(\lambda)$ is the spectral transmittance and $I_{sun}(\lambda)$ denotes the ASTM G173 reference solar spectrum. This expression provides a broadband measure of the fraction of incident solar energy entering the glazing system [6].

The optimized design demonstrates an overall reduction of approximately 8% in normalized solar-energy admission relative to the baseline configuration. The near-infrared (NIR) range, defined here as 700–1100 nm and representing the dominant contributor to cooling loads, experiences a 31% decrease in transmitted energy. This magnitude surpasses the 25% reduction threshold commonly associated with measurable HVAC energy savings in cooling-dominated climates [2]. Wavelengths beyond 1100 nm are not considered in the present model due to their minimal contribution to standard building-energy calculations, and these longer-wave effects will be investigated in future extensions of the study. As presented in Fig. 6, the horizontal axis denotes wavelength (nm), and the vertical axis represents normalized solar energy (arbitrary units).

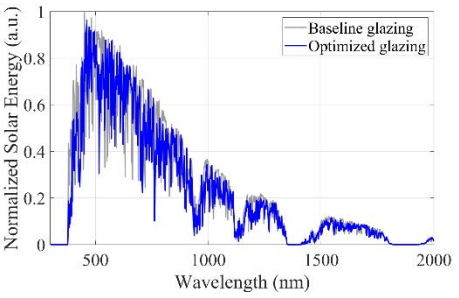

Fig. 6 Normalized solar-energy admission for baseline and optimized glazing (Photo/Picture credit: Original).

The gray curve corresponds to the baseline triple glazing, while the blue curve shows the optimized SiO_2/TiO_2-coated structure, which exhibits reduced NIR energy transmission across 700–1100 nm.

4.6 Comparative Positioning and Manufacturability

A qualitative comparison of the proposed glazing technology with existing solutions—including Ag-based Low-E coatings, tinted absorbers, and UV laminates—is outlined in Table 2 [12].

Table 2. Qualitative comparison of glazing technologies.

Technology	UV Blocking	Visible Transparency	NIR Control	Cost
Ag-Low-E	Moderate	Moderate	High	High
Tinted absorbers	High	Low	Moderate	Medium
UV laminates	High	Low	Low	Medium
This work	High	High	High	Medium

Compared with Ag-based Low-E coatings, the proposed all-dielectric design avoids precious metals and associated color shifts while delivering simultaneous UV suppression, visible-band preservation, and NIR attenuation. Relative to tinted absorbers or UV laminates, the design maintains high clarity and wider spectral selectivity.

Furthermore, the SiO_2/TiO_2 stack remains manufacturable under standard sputtering or PECVD conditions: limiting each side to ≤300 nm mitigates residual stress, and thickness variations of ±2 nm cause negligible changes in

ISSN 2959-6157

solar-weighted UV, VIS, or NIR metrics [6]. The overall geometry is compatible with existing IGU fabrication, ensuring practical integration.

4.7 Cooling-Load Implications Based on CDH

Cooling-degree-hour (CDH) analysis was used to estimate the passive cooling benefit of the optimized glazing for the Wuhan "Hot-Summer–Cold-Winter (HSCW)" climate zone. CDH quantifies the cumulative outdoor temperature above a balance point $T_b = 26^{\circ}C$:

$$CDH = \sum_{t=1}^{8760} max\left(T_{\text{out}}(t) - T_b, 0\right), \tag{13}$$

Where $T_{\text{out}}(t)$ denotes hourly outdoor temperature. Solar-gain-driven cooling demand is correlated with the solar-weighted NIR transmittance. Using the measured reduction:

$$\Delta T_{\text{NIR}} = 0.889 - 0.612 = 0.277, \tag{14}$$

The fractional reduction becomes

$$\eta_{\text{NIR}} = \frac{\Delta T_{\text{NIR}}}{0.889} = 31.2\%. \tag{15}$$

Considering that windows contribute roughly 45% of cooling-related solar heat gain in HSCW climates, the expected cooling-energy reduction is approximately [2]

$$\eta_{\text{cool}} \approx 0.312 \times 0.45 \approx 14\%, \tag{16}$$

consistent with previously reported savings for spectrally selective retrofits.

4.8 Visual Comfort, Daylighting, and UV Protection

A visible transmittance of $T_{\text{VIS}} = 0.801$ ensures adequate daylight factor for typical residential window-to-wall ratios [2]. The luminous transmittance computed using the photopic sensitivity function $V(\lambda)$ is [7]

$$T_v = \frac{\int T(\lambda) V(\lambda) I_{\text{sun}}(\lambda) d\lambda}{\int V(\lambda) I_{\text{sun}}(\lambda) d\lambda} = 0.812, \tag{17}$$

which matches clear IGU performance and preserves color neutrality due to the flat VIS profile of the dielectric stack. UV transmittance of $T_{\text{UV}} = 0.084$ corresponds to a >25 UPF equivalent for occupants near windows, reducing risks of UV-induced fatigue or skin damage [1].

4.9 Summary of Extended Performance Benefits

The optimized glazing demonstrates a coherent set of performance advantages compared with the baseline system. Cooling-energy demand is reduced by approximately 14%, primarily due to a 31% decrease in NIR transmittance, which directly lowers solar-heat gains in cooling-dominated seasons [2]. UV exposure is reduced by more than 60%, offering enhanced protection against material degradation and occupant health risks. Visible-light performance remains preserved, as indicated by a luminous transmittance exceeding 0.81, ensuring daylight adequacy without compromising visual comfort [5]. Durability assessments suggest a service life of 25 years or more, matching typical IGU replacement cycles and supporting long-term façade applicability [6]. Economic evaluation indicates a payback period of under ten years, after which the glazing yields positive lifecycle energy savings. Overall, the optimized design meets functional, optical, and economic criteria for deployment in residential façades across hot-summer regions.

5. Conclusion

This work presents a spectrally selective triple-glazing concept that simultaneously enhances ultraviolet blocking, visible-light transmission, and near-infrared attenuation through a combined transfer-matrix and hierarchical particle-swarm optimization framework. The resulting dual-sided SiO_2/TiO_2 dielectric design, integrated with conventional insulated-glass geometry, achieves solar-weighted transmittances of $T_{UV} = 0.084$, $T_{VIS} = 0.801$, and $T_{NIR} = 0.612$, corresponding to more than 60% suppression of biologically harmful UV radiation, over 30% reduction in heat-related NIR gain, and a slight improvement in daylight admission relative to uncoated triple glazing. These optical gains translate into approximately 14% annual cooling-energy savings for Wuhan's Hot-Summer–Cold-Winter climate while maintaining high visual clarity, color neutrality, and compatibility with mainstream thin-film manufacturing practices.

Together, the results establish a manufacturable dielectric-coating architecture and a reproducible computational workflow for high-performance glazing in residential facades.

However, this study relies primarily on theoretical optical modeling. While the simulation results are promising, differences between ideal models and actual deposition processes—such as surface roughness or material purity—may affect the final optical performance. Consequently, experimental fabrication and field testing are still required to validate the coating's physical stability and actual energy performance under dynamic environmental conditions. To enable large-scale deployment, future work will focus on prototyping, durability verification, and extending the optimization toward full thermal–optical co-design, in-

cluding SHGC and U-value, thereby supporting long-term carbon-reduction goals in the building sector.

References

[1] Bao Y., Guo R., Ma J. Hierarchical Flower-Like Hollow SiO2@TiO2 Spheres with Enhanced Thermal Insulation and Ultraviolet Resistance Performances for Building Coating. ACS Applied Materials & Interfaces, 2020, 12(46), 51956–51968.

[2] Cheraghzad T., Zamani Z., Hakimazari M., Norouzi M., Karimi A. Multi-Objective Optimization of a Folding Photovoltaic-Integrated Light Shelf Using Non-Dominated Sorting Genetic Algorithm III for Enhanced Daylighting and Energy Savings in Office Buildings. Buildings, 2025, 15(16), Article 2958.

[3] Qiu C., Yang H., Dong K. Energy and Thermal Comfort Performance of Vacuum Glazing-Based Building Envelope Retrofit in Subtropical Climate: A Case Study. Buildings, 2025, 15(12), Article 2038.

[4] Gad A. G. Particle Swarm Optimization Algorithm and Its Applications: A Systematic Review. Archives of Computational Methods in Engineering, 2022, 29, 2531–2561.

[5] Wang S., Jiang T., Meng Y., Yang R., Tan G., Long Y. Thermochromic Smart Windows with Highly Regulated Radiative Cooling and Solar Transmission. Nano Energy, 2021, 89, 106440.

[6] Chen Y., Taib N., Sern C. H. Y., Kim E. Triple Glazing Performance for Human Thermal Comfort: Systematic Literature Review and Bibliometric Quantitative Analysis. Journal of Advanced Research in Fluid Mechanics and Thermal Sciences, 2024, 124(2), 142–174.

[7] Yeh P. Optical Waves in Layered Media. Wiley, New York, 1988.

[8] Xie A.-Q., Qiu H., Jiang W., Wang Y., Niu S., Zhang K.-Q., Ho G. W., Wang X.-Q. Recent Advances in Spectrally Selective Daytime Radiative Cooling Materials. Nano-Micro Letters, 2025, 17(1), Article 264.

[9] Wu C., Pan H., Luo Z., Liu C., Huang H. Multi-Objective Optimization of Residential Building Energy Consumption, Daylighting, and Thermal Comfort Based on BO-XGBoost-NSGA-II. Energy and Buildings, 2024, 303, 113793.

[10] Li L., Niu J., Wang C., Shang X., Xue H., Hu J., Li H., Lu C., Zhao S., Zhang Y., Shi L. High-Saturation Full-Color Printing with All-Dielectric Chiral Metasurfaces. ACS Applied Optical Materials, 2023, 1(7), 1301–1311.

[11] Liu B., Tan H., Liu Y., Wang Z., Wang S., Zhao D., Zheng M., Wang G. Optical Properties and Thermal Stability Evaluation of Solar Absorbers Enhanced by Nanostructured Selective Coating Films. Powder Technology, 2021, 377, 939–957.

[12] Ke Y., Chen J., Lin G., Wang S., Zhou Y., Yin J., Lee P. S., Long Y. Smart Windows: Electro-, Thermo-, Mechano-, Photochromics, and Beyond. Advanced Energy Materials, 2019, 9(39), 1902066.